Meten is weten

"To measure is to know"

Dutch proverb

Fracture experiments

4 FRACTURE EXPERIMENTS

This chapter contains the results and analysis of the experimental work performed according to the research methodology presented in the previous chapter. The main objectives of the chapter are to determine the fracture properties, to study size effect, and to explore the fatigue behaviour of the high performance fibre reinforced material.

The general engineering properties determined for the materials tested in the different phases are presented in Section 4.1. The data processing and presentation techniques used for the flexural test are discussed in Section 4.2. The outcomes of the size effect study on the high performance fibre reinforced material are presented in Section 4.3. In Section 4.4, a method is developed to determine the specific fracture energy G_f from TPB experiments. Another key fracture property of the material, the tensile strength (f_t), is determined from an adjusted tensile splitting procedure in Section 4.5. The results of the cyclic flexural tests are analysed in Section 4.6, followed by a discussion on the main findings of the experimental work in Section 4.7.

4.1 Engineering properties

The average results for the compressive strength (f_c), Young's modulus (E) and Poisson's ratio (v) for all mixes are shown in Table 4-1. These general engineering properties were obtained using the procedures discussed in Section 3.2.5. The results for the f_c, are based on six specimens per mix type, the results for E and v are based on three tests per mix types.

The results for the high performance concrete mix designs (A, B, D, E) show an upward trend in the values of the f_c and E with time. This was unintentional. The mix designs did not change significantly for the different phases. The increase of the f_c is believed to be a function of changes in cement quality over the course of the project. During this time period similar trends were observed in experiments on concrete at the UP laboratory unrelated to this project.

Table 4-1: Average engineering properties for all studied mixes

	f_c [MPa]	Std.dev. [MPa]	E [GPa]	Std.dev. [GPa]	v	Std.dev.
Mix A	108.9	7.4	49.6	0.5	0.14	0.023
Mix B	115.5	4.9	46.3	0.3	0.16	0.012
Mix C	40.8	4.4	31.2	6.4	0.20	0.040
Mix D	125.5	4.7	49.7	0.7	0.17	0.005
Mix E	137.2	6.0	62.9	0.7	0.15	0.005

4.2 Presentation of monotonic flexural test results

The results of all flexural tests under monotonic loading conducted as part of this study are presented in Appendix A. The results are plotted in terms of load versus vertical displacement as measured during the test using LVDTs. A typical example of such a curve is shown in Figure 4-1a. In the later experimental phases, the CMOD was recorded in addition to the vertical displacement for the notched TPB specimens. An example of a load-CMOD curve is shown in Figure 4-1b.
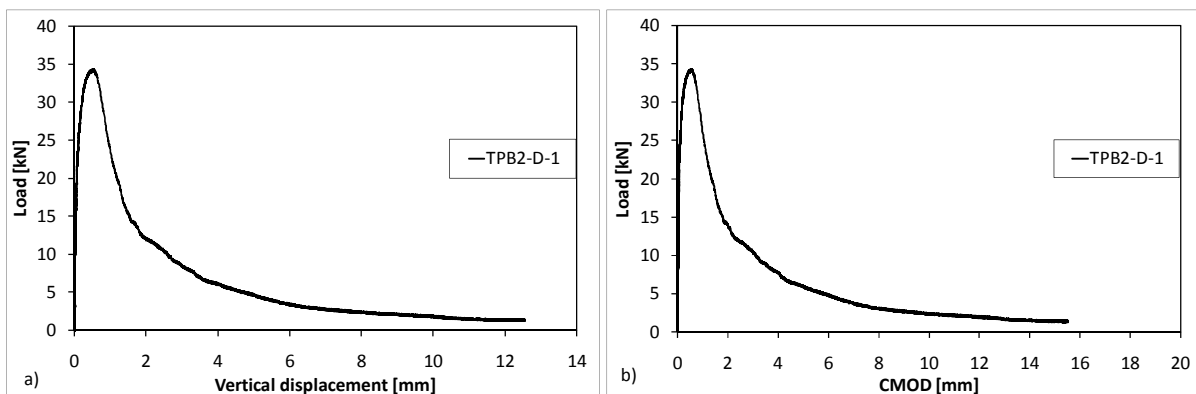

Figure 4-1: Example of load-displacement curve, b: Example of load-CMOD curve

The test matrix contains specimens with and without weight correction. A weight corrected specimen has a length of twice the size of the span thus, the initial moment due to self weight at the centre of the span is approximately zero. If a specimen is tested without weight correction, a load due to self weight is introduced when the specimen is placed in the test rig. The influence of this offset in load on the flexural capacity of the beam will not be captured in the load-deflection curve of the subsequent bending test unless a correction is made. To take the initial load P_0 due to self-weight into account, the load-displacement curve for these tests is shifted up by:

$$P_0 = \frac{4M_0}{s} \tag{4.1}$$

Where M_0 is the bending moment at centre span due to self weight, calculated assuming a density of 2500 kg/m^3 for the material. Where required, the results for flexural tests on beams presented in this document have been corrected for self weight using this procedure. The corrected load-displacement curves are used to evaluate the flexural results for size effect in Section 4.3 and from them the specific fracture energy is determined in Section 4.4.

4.3   Size effect

According to linear elastic limit state design theory, failure will occur when a certain critical level of stress or strain is reached in a structural element, regardless of the size of the element. Under this assumption it should be possible to use the elastic limit determined for a flexural beam test, to for example predict the peak load of a slab in flexure. As discussed in Chapter 2, this approach is known to have limitations for application to concrete, due to the occurrence of size effect. In this section, size effect in the UTCRCP material is quantified. To this aim, beam and disk specimens of different sizes were tested while maintaining geometry.

4.3.1   Size effect in flexural beam tests

Table 4-2 shows the ultimate nominal stress (σ_{Nu}) results per specimen type for the different mixes. The nominal stress (σ_N) (at any load level) is calculated for FPB tests using Equation 2.1 and for TPB tests using Equation 2.2 introduced earlier in the document. The table shows that for each mix type the average value of σ_{Nu} varies for the different sizes and

test configurations (i.e. TPB, FPB). To investigate the size dependency of σ_{Nu}, specimens of different sizes were tested while maintaining the geometry. These series of specimens tested as part of phase three and four (Mixes D and E) have different heights, but a constant span to height (s/h) and notch dept to height (s/a) ratios. For the tests on Mix E specimens geometry was maintained in all three dimensions, i.e. the width to height ratio (b/h) was also kept constant. The results of the size effect investigation discussed below were published as part of this study in Denneman et al. (2010a) and Denneman et al. (2010b).

Table 4-2: σ_{Nu} results flexural beam tests

Specimen type	s/h	a/h	b/h	σ_{Nu} [MPa]	Std.dev. [MPa]	Number of specimens
Mix A						
TPB1-A	3 1/3	1/6	1	13.3	1.08	3
TPB2-A	4		1	13.5	1.27	3
TPB3-A	6 2/3	1/3	2	11.3	1.76	3
TPB4-A	10		2	13.9	0.89	3
FPB1-A	4		1	10.9	0.84	3
Mix B						
TPB1-B	4		1	13.9	1.45	3
TPB2-B	6 2/3	1/3	2	13.4	1.83	3
TPB3-B	10		2	14.7	1.43	3
FPB1-B	4		1	11.7	0.84	3
Mix C						
TPB1-C	4	1/3	1	4.7	0.18	3
Mix D						
TPB1-D	3 1/3	1/3	3	17.9	2.30	2
TPB2-D	3 1/3	1/3	1	15.2	0.43	3
TPB3-D	3 1/3	1/3	2/3	13.1	1.45	3
FPB1-D	3		1	14.0	0.56	3
FPB2-D	3		2/3	12.0	0.85	3
Mix E						
TPB1-E	3	1/3	1	10.9	0.81	5
FPB1-E	3		1	12.9	1.35	5
FPB2-E	3		1	14.3	0.66	5
FPB3-E	3		1	14.5	1.49	5

Figure 4-2a shows the average load displacement curves for TPB tests on mix D specimens. The figure shows the large post-peak bearing capacity of fibre reinforced concrete. The peak load required to break the specimen increases with the size of the beam as expected. When the nominal stress (σ_N) for the beams is plotted against the deflection (δ) as a ratio of the effective beam height (h-a), a clear size effect as discussed in Section 2.4.2 appears. This is shown in Figure 4-2b. The graphs show the effect of size on the peak load as well as the post peak load capacity of the material. In the figure, the nominal strength of the material

increases with a decrease in size. This is of course not related to a real increase in strength of the material, but rather a manifestation of the limitations to LE calculation of the stress condition in the beam specimens.
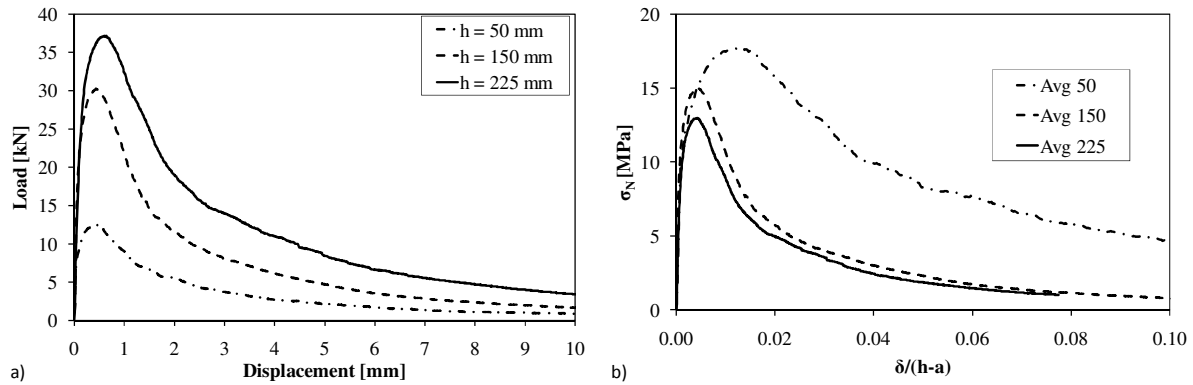

Figure 4-2a) Average load displacement curves for monotonic TPB tests mix D, b) Nominal stress versus relative displacement Mix D specimens.

A comparison of the σ_{Nu} values for TPB and FPB specimens of different sizes is plotted in Figure 4-3a for Mix D and in Figure 4-3b for mix E. The Mix D specimens show similar size effect trends in σ_{Nu} for the TPB and FPB. The results indicate a statistically significant (95% confidence) size effect in σ_{Nu} for both test configurations. The results for the FPB tests on Mix E specimens, shown in Figure 4-3b, also show a statistically significant size effect. The trend is however less steep, in particular between the 50 mm and 100 mm specimens. One of the reasons for this phenomenon may lie in the geometry of the specimens. In the first phase of the size effect experiment (Mix D) the width of the specimen was kept constant for the different beam heights. In the second phase (Mix E) the width was scaled as well in accordance to the span to depth ratio. The fracture mechanics size effect for Mix E may have become obscured due to the boundary layer effect. As the boundary layer contains mainly small sized material it will contain less steel fibres. Furthermore the steel fibres need a certain cover to function properly. Due to the limited width, the 50x50 specimens will have a relatively larger boundary layer than the larger 100x100 mm and 150x150 mm specimens.
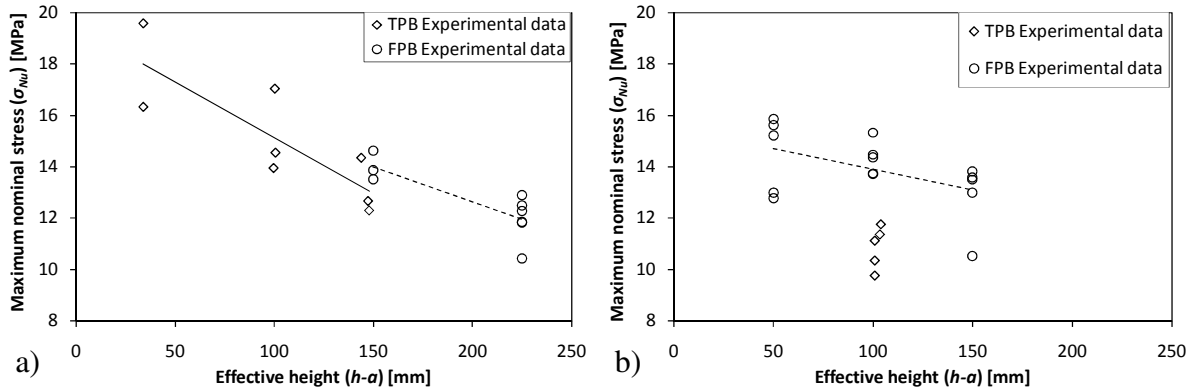
Figure 4-3a) Size effect in σ_{Nu} results for mix D, b) Size effect in σ_{Nu} results for mix E

4.3.2 Comparison of size effect results against published data for plain concrete

In the previous section it was shown that the σ_{Nu} for the high performance fibre reinforced concrete is subject to considerable size effects. The material differs from plain concrete in terms of its high compressive strength and substantial post crack stress transfer capacity. These characteristics may influence the magnitude of the size effect in the material compared to plain concrete. The size effect in the high performance material will be compared to the size effect of plain concrete recorded in literature. The relative magnitude of the size effect will determine whether LE design approaches are more or less applicable to the high performance concrete material than to plain concrete.

Bažant and Li (1995) collated the results of a number of size effect studies on plain concrete. In this publication a linear regression was fitted to the size effect results from the historic data.

$$\sigma_{Nu(I)} = c_1\left(1 + \frac{c_2}{h_I}\right) \tag{4.2}$$

Where $\sigma_{Nu(I)}$ is the nominal maximum stress in pounds per square inch, c_1 and c_2 are regression constants, h_I is the height of the specimen in inches. For a number of studies with specimen sizes in the range used for this study, the regression equations, converted to SI units are shown in Figure 4-4. Also plotted in the figure is a regression for the data produced by this study. The curve was fitted using the Microsoft excel solver. The plot allows a comparison of size effect in plain concrete and the high performance fibre reinforced concrete used for this work. To be able to compare the size effect relative to the σ_{Nu} value for the standard 150 mm MOR test, the ratio of σ_{Nu}/MOR is shown in Figure 4-5.

The figures show that in absolute terms the size effect of the UTCRCP material is higher than that of plain concrete. The size effect in the UTCRCP material relative to the value of the standard MOR test is comparable to what can be expected in plain concrete.
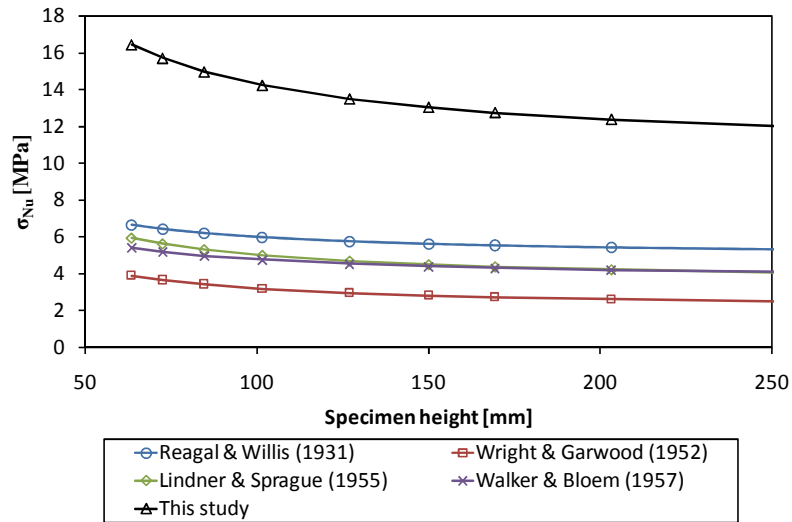

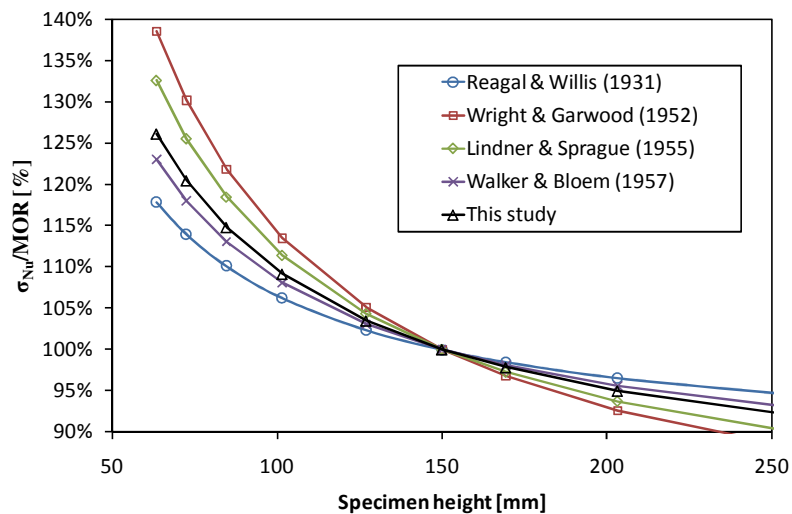**Figure 4-4: Linear regression for size effect in this and other studies.**

Figure 4-5: Relative size effect in studies normalized for MOR standard size specimen

4.3.3 Size effect in flexural disk tests

As discussed in Chapter 2, size effect has been linked to the underestimation of the carrying capacity of slabs when the calculation is based on beam MOR results and linear elastic analysis. This phenomenon becomes apparent in the analysis of the flexural disks tested as

part of experimental phase one and four. The load-displacement curves for the disks are contained in Appendix A.

The typical mode of failure for the disk specimens is cracking at midspan between the supports, forming the pattern shown in Figure 4-6. As the cracking pattern is instrumental to the analysis, test results were rejected in cases where the cracks formed elsewhere. Dupont and Vandewalle (2004) showed that yield line analysis can be used to relate the loading of the disks to the moment capacity of the specimens.
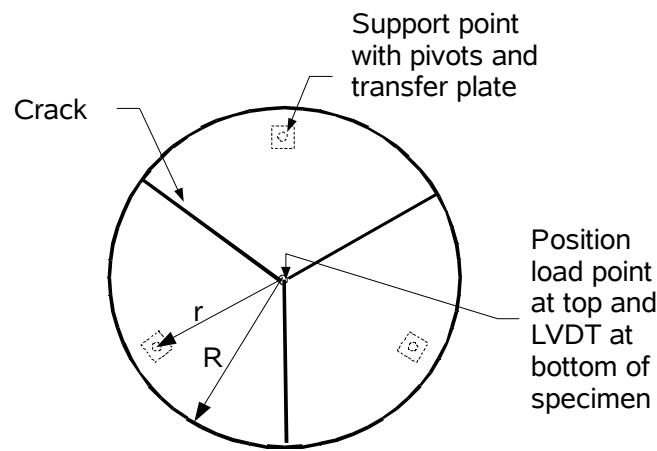

Figure 4-6: Typical crack pattern in disk experiments

Assuming that yielding takes place at the same time along the full length and depth of the lines shown in the sketch, the moment capacity (M_u) is given by:

$$M_u = \frac{P_u r}{6R \cos 30°} \tag{4.3}$$

Where P_u is the peak load, r and R are the radii from the centre of the disk centre to the centre of the support and from the centre of the disk to the edge of the disk, respectively. Assuming a linear elastic stress distribution at failure Barnett et al. (2010) equate the stress distribution disk to that in a beam of the same height by stating:

$$M_u = \frac{P_u r}{6R \cos 30°} = \frac{\sigma_{Nu} h^2}{6} \tag{4.4}$$

Which allows:

$$\sigma_{Nu} = \frac{P_u r}{h^2 R \cos 30°}$$

(4.5)

The ultimate nominal stress (σ_{Nu}) values calculated for the disks using the above equations are shown in Table 4-3. The 55 mm and 70 mm high specimens are geometrically similar as there is only slight difference in the radius to height (r/h) ratio. The σ_{Nu} values are consistent for the different sizes and mix types. The results do not show a statistically significant size effect between the 50 and 70 mm high disk specimens for either mix. The reason for this may be the relatively small difference in specimen size. The test matrix for the disk specimens was not designed with a size effect study in mind. Comparison of the σ_{Nu} for the disks in Table 4-3 to the σ_{Nu} values from flexural tests on beams in Table 4-2 shows that the values for σ_{Nu} for the disks are on the high side of the result spectrum for Mix A and B.

Table 4-3: σ_{Nu} results flexural disk tests

Specimen type	r/h	σ_{Nu} [MPa]	Std. dev. [MPa]
Disk1-A	0.20	13.8	0.2
Disk2-A	0.19	13.9	1.0
Disk1-B	0.20	14.1	1.0
Disk2-B	0.19	13.7	1.3

Note here however, that the stresses in the disks were calculated using plastic yield line theory instead of the LE analysis applied to concrete pavements. In LE analysis of the disks stresses are not distributed evenly along the eventual yield lines. Consequently, the stresses in LE analysis may be expected to be significantly higher than the σ_{Nu} values shown in Table 4-2. To get a full appreciation of the size effect between the LE analysis of beams and disks, numerical simulation is required, which will be performed in the next chapter.

4.4 Fracture energy

The specific fracture energy G_f is a key fracture mechanics parameter to be determined for use in numerical simulation of crack propagation. As part of this study, a detailed analysis

method was developed to determine G_f for FRC. The fracture energy is determined from TPB flexural tests performed in the different phases as described in Section 3.2.

4.4.1 Work of fracture and fracture energy

The work of fracture W_f required to completely break a specimen in a flexural test is represented by the area under the load-displacement or load-CMOD curve. Figure 4-7 shows the load-displacement curves obtained for the first group of specimens tested as part of this study, i.e. TPB1-A. An important assumption of this study is that the effect of the synthetic and steel fibres is distributed equally over the fracture area. The composite fibre concrete material behaves as a homogeneous material and the fibres do not need to be handled as separate entities. The energy required to produce a unit of fractured area is G_f, which is calculated for the concrete-fibres composite material using Equation 4.6:

$$G_f = \frac{W_f}{b(h-a)} \tag{4.6}$$

where b is the width of the sample, h the total sample height and a the notch depth.
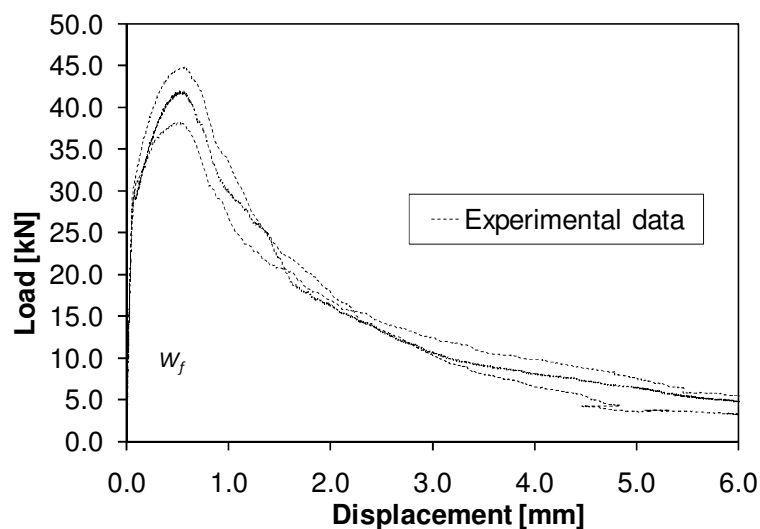

Figure 4-7: Load-displacement curves for specimens type TPB1-A

Some of the specimen tested in phase I contained reinforcement in the form of steel bars (rebar) in addition to steel fibres. The influence of the inclusion of the reinforcement bars on the work required to break the sample is shown in Figure 4-8. The additional work W_{rebar}

required, at a specific fibre content, to break the samples with steel bars can be calculated from the average value $W_{f(rebar)}$ for samples with both fibres and rebar, and the average value W_f for samples with fibres only:

$$W_{rebar} = W_{f(rebar)} - W_f \qquad\qquad (4.7)$$

It is of course impossible to express the additional work required to break specimen with reinforcement bars in terms of G_f, as the bars are not homogeneously distributed over the cross-sectional area.
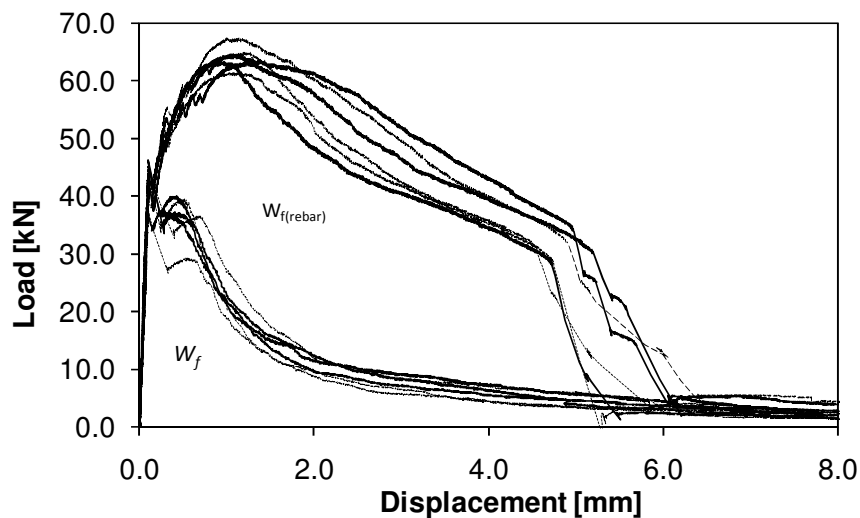

Figure 4-8: TPB on results on samples with and without rebar

4.4.2 Modelling of the load-displacement tail

The fibre reinforced concrete under study behaves ductile when compared to plain concrete. To obtain the full work of fracture from the TPB test, the specimen needs to be broken completely. This requires all steel fibres over the ligament area to be pulled out right to the top of the beam. For the 30 mm long steel fibres used in this study this would require a theoretical crack width of 15 mm at the top of the beam. The large rotation of the two beam halves needed to achieve this cannot be reached in the normal TPB test setup.

TPB tests on fibre reinforced concrete will therefore generally be stopped before the beam is fully broken. As a result a part of the tail of the load-deflection curve will be missing, as can

be observed in Figure 4-1 and Figure 4-8. The figure shows that after the peak, the load moves asymptotically to zero. At the final stage of the experiment the load has reduced significantly, but the specimens have not broken into two halves completely and the full work of fracture has not been recorded. If the results have been corrected for self weight, the upwards shift of the load displacement curve adds to the portion of the load-displacement tail that is missing from the recorded data.

To calculate the full work of fracture and get a precise measure of G_f, it will be necessary to model the missing part of the load deflection curve. A methodology is proposed that draws from the work on plain concrete published in Elices et al. (1992), Elices et al. (1997), Bažant and Planas (1997) and Rosselló et al. (2006).

Near the end of the test, the crack has propagated to the top of the beam and the crack mouth has opened considerably. The neutral axis of the stress distribution shifts ever closer to top of the beam as the size of the compressive zone reduces during the test. In this situation, the beam can be modelled as two ridged parts rotating around a point at the top of the beam at centre span, as shown in Figure 4-9a.
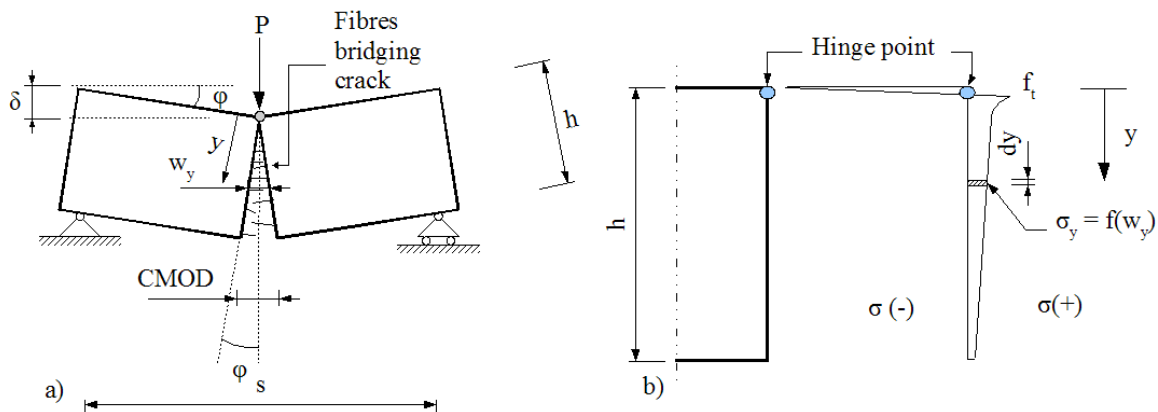

Figure 4-9a: Kinematic model of TPB test at large deflections, b: Stress distribution in kinematic model (not to scale)

For fibre reinforced concrete this situation will exists for a considerable longer period than for plain concrete, while the fibres bridging the crack are being pulled out. The angle of

rotation (φ) around the hinge point at the top of the beam at any value of deflection (δ) is obtained from:

$$\tan\varphi = \frac{2\delta}{s} \Rightarrow \varphi \approx \frac{2\delta}{s} \qquad (4.8)$$

The crack width at any depth (y) of the beam near the end of the test is calculated from:

$$w_y = 2y\sin\varphi \approx 2y\varphi \qquad (4.9)$$

It can be shown that the kinematic model of the beam in Figure 4-9a is accurate, by comparing the horizontal crack opening displacement at the mouth of the notch calculated using the model, to the CMOD measured with a clip gauge for tests in which both the CMOD and vertical displacement were recorded. At large rotations the recorded CMOD and the crack mouth opening calculated using the kinematic model in Figure 4-9a reach unity, i.e.:

$$\frac{2h\sin\varphi}{CMOD} = 1 \qquad (4.10)$$

For the beam data shown in Figure 3, unity is reached at approximately 2 mm deflection, implying that after 2 mm the kinematic model is valid for the data.
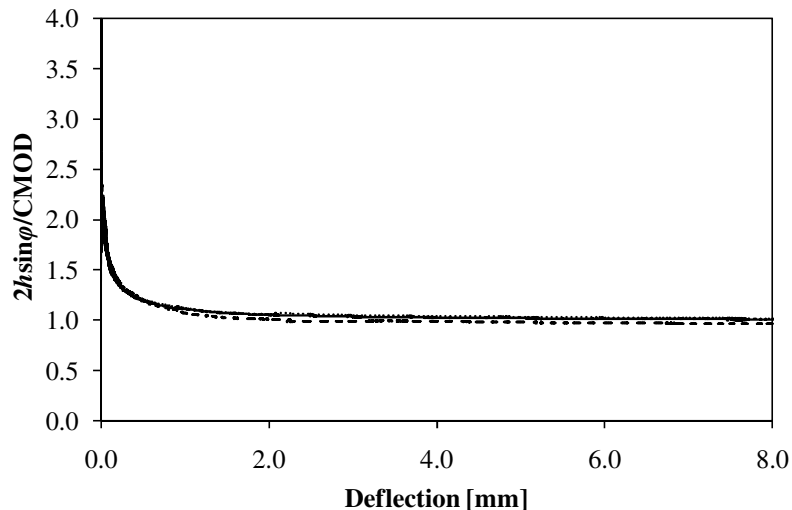

Figure 4-10: Comparison of recorded CMOD and crack mouth opening calculated using the kinematic model in Figure 4-9a.

The stress distribution in the beam at large rotations may be approximated by assuming that the depth of the compressive zone is negligible and concentrated at the hinge point (Elices et al., 1992). The post crack softening behaviour of the material can be described using a cohesive crack approach as introduced for concrete by Hillerborg et al. (1976). Under the assumption of a cohesive crack, the material behaves elastically until the stress reaches the tensile strength (f_t) of the material. At this point a crack is formed. Stresses are transferred over the crack according to a softening function. The crack bridging tensile stress (σ_y) at any point (y) along the depth of the cracked beam shown in Figure 4-9b is written as a function of the crack width (w_y) at that position

$$\sigma_y = \mathrm{f}(w_y) \tag{4.11}$$

Regardless of the shape of the softening function, the moment capacity in the kinematic model can be written as the integral of the softening function times the lever arm to the top of the beam:

$$M = \int_0^h \sigma(w_y) b y \, \mathrm{d}y \tag{4.12}$$

Substituting w_y in Equation (4.12) by the function in Equation (4.9) results in:

$$M = \frac{b}{(2\varphi)^2} \int_0^{w_c} \sigma(w_y) w_y \, \mathrm{d}w \tag{4.13}$$

where w_c is the crack width opening position at which the softening is complete and $\sigma = 0$. Note that for exponential softening $w_c = \infty$. Following Elices et al. (1992), the integral in Equation (4.13) is defined as parameter A:

$$A = \int_0^{w_c} \sigma(w_y) w_y \mathrm{d}w \tag{4.14}$$

With this, Equation (4.13) may be written as:

$$\frac{M}{b} = \frac{A}{(2\varphi)^2} \tag{4.15}$$

This defines a relationship between the remaining moment capacity (M) in the beam at large displacements, and the angle of rotation (φ). Parameter A can be calculated without having to define the shape of the softening curve, as A corresponds to the slope of a graph plotting M/b against $(2\varphi)^{-2}$. The behaviour of parameter A at large rotations (small values of $(2\varphi)^{-2}$), where it becomes a constant, is shown in Figure 4-11a for data obtained from TPB tests performed as part of this study. A was determined per specimen type using least squares fitting. Bažant and Planas (1997) propose that A is a size independent material property for plain concrete. This would imply that the fracture energy G_f is a true material property as well. Figure 4-11b shows the behaviour of A for the different specimen sizes tested for mix B. Parameter A has a similar value for different specimen sizes of the same material. It is possible that A is size independent for fibre reinforced concrete. The limited number of specimens tested per size and mix type in this study does however not allow a statistical test of the hypothesis that A is size independent.
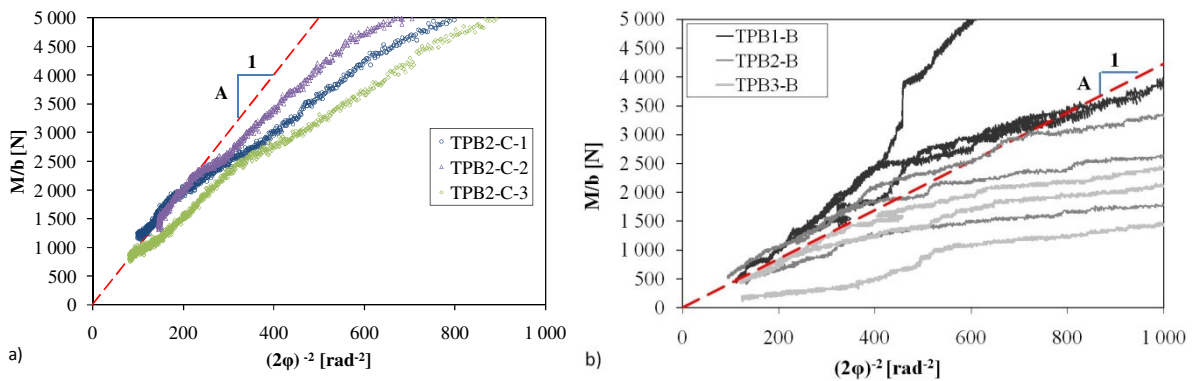

Figure 4-11a: Determination of A for single specimen type, b: Determination of A for different sizes of Mix B specimens.

Once A has been determined the missing part of the asymptotic tail of the displacement curve can be modelled by combining Equations (4.8) and (4.16) which allows calculation of P_{tail} for any δ.

$$P_{tail} = \frac{bsA}{4\delta^2} \qquad , \qquad\qquad (4.16)$$

78

An example of a load-deflection curve with a modelled tail end is shown in Figure 4-12. The modelled tail provides a close fit to the path of the experimental tail. The curve can now be extrapolated to infinity. The total work of fracture is calculated by adding the area under the modelled tail of the curve to the area under the known part of the curve. The work under the modelled tail is determined from:

$$W_{tail} = \int_{\delta_{end}}^{\infty} P\mathrm{d}(\delta) = \frac{bsA}{4\delta_{end}} \tag{4.17}$$

Where, δ_{end} is the deflection at the last available experimental data point. The total W_f can be calculated by adding W_{tail} to the area under the experimental load-deflection curve. G_f can be obtained using Equation 4.6.
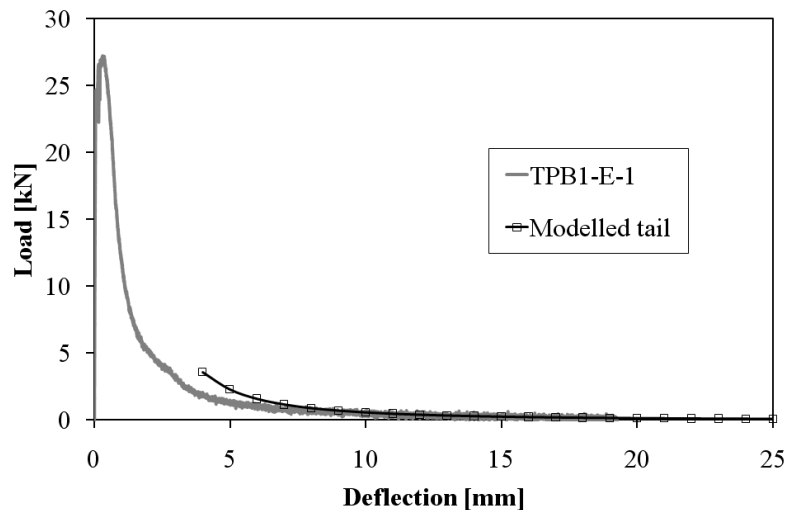

Figure 4-12: Load-displacement curve with modelled tail

The average values for A, W_f, W_{tail}, W_{rebar} and G_f for the TPB experiments on the different mixes are shown in Table 4-4. According to the proposed model, approximately 18 per cent (on average) of the work of fracture was still available under the missing part of the tail when the tests were stopped (for beams without rebar).

The results obtained in this study do not indicate a statistical size-effect in the value of G_f. Due to the variability inherent to the material and TPB results, a large number of specimens would have to be tested in order to verify whether any size effect in G_f occurs.

The differences in the fracture energy of mixes produced at different fibre contents is evident from the results. Mixes B and D, produced at 120 kg/m^3 steel fibre content have a significantly higher specific fracture energy than mixes A and E, produced with 80 kg/m^3 steel fibres.

The methodology developed in this study to determine the fracture energy was published in Denneman et al (2011a).

Table 4-4: Summary of work of fracture results

Specimen type	A [Nmm rad^2]	W_f [Nmm]	W_{tail} [%]	W_{rebar} [Nmm]	G_f [N/mm]	Std.dev. [N/mm]	Number of specimens
Mix A							
TPB1-A	9.74	1.23E+05	17.6%		6.57	0.96	3
TPB2-A	4.96	8.54E+04	12.0%		4.56	0.69	3
TPB3-A	4.59	3.70E+04	22.2%		4.93	1.10	3
TPB4-A	2.97	2.86E+04	16.5%		3.82	0.88	3
TPB5-A		3.26E+05	8.49%	1.98E+05			3
TPB6-A		2.71E+05	8.47%	1.96E+05			3
TPB7-A		1.86E+05	30.4%	9.00E+04			3
TPB8-A		2.00E+05	44.9%	2.33E+01			3
Mix B							
TPB1-B	8.36	9.97E+04	15.7%		5.32	0.31	3
TPB2-B	4.34	4.13E+04	21.0%		5.51	1.21	3
TPB3-B	5.22	4.23E+04	21.2%		5.64	1.37	3
TPB4-B		2.70E+05	6.7%	1.68E+05			3
TPB5-B		2.26E+05	41.5%	9.98E+04			3
TPB6-B		2.19E+05	43.8%	9.02E+04			3
Mix C							
TPB1-C	0.10	3.21E+03	22.4%		0.211	0.033	3
Mix D							
TPB1-D	13.99	4.26E+04	19.2%		8.34	0.24	3
TPB2-D	11.38	9.66E+04	15.0%		6.41	0.63	3
TPB3-D	15.23	1.62E+05	17.8%		7.41	0.86	3
Mix E							
TPB1-E	11.61	5.43E+04	19.0%		3.53	0.50	5

4.4.3 Tensile splitting results

The split cylinder tests were performed using the adjusted test procedure as discussed in Section 3.2.6. The load-transversal deformation curves obtained for the cylinder splitting tests performed as part of this study are shown in Figure 4-13. The observed material behaviour is comparable to the graph shown in Figure 3-8c. Two separate peak load conditions are reached during the test. An important finding for the tensile splitting tests performed on FRC as part of the study is that with the second peak is higher than the first peak.
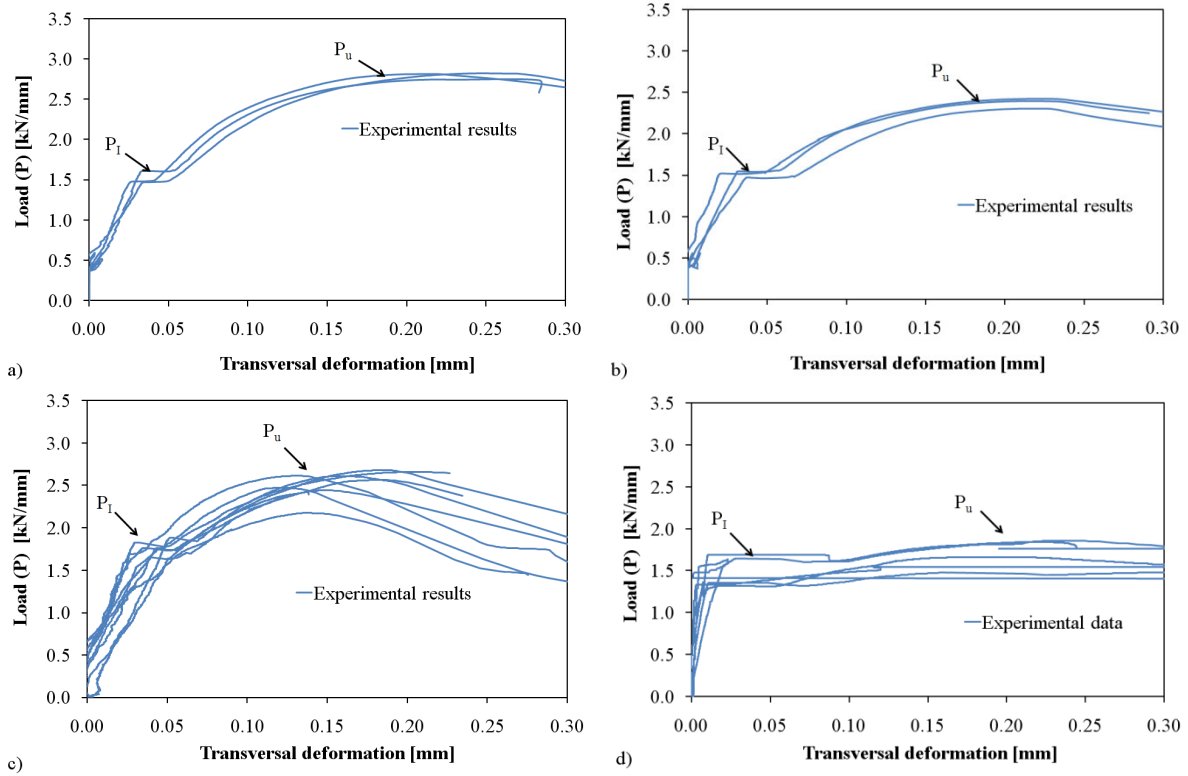
Figure 4-13: Load-transversal deformation curves for cylinder splitting tests on: a: Mix A specimens, b: Mix B specimens, c: Mix D specimen and d: Mix E specimens,

The figures indicate that the material behaves linear elastically until a first peak is reached at load level (P_I). At this point a crack is introduced. The load stabilizes at this level before increasing again with an increase deformation. Eventually a second and higher peak load (P_u) is reached. In conventional splitting tests, this second, ultimate peak load is the only value that would be recorded. Using the approach in conventional test methods, the nominal ultimate tensile stress σ_{Nu} would be calculated using the relationship in Equation 3.1:

$$\sigma_{Nu} = \frac{2P_u}{\pi D} \tag{4.18}$$

The results of this study, indicate that P_u is related to a secondary cracking mechanism in the tests and not to linear elastic tensile stress distribution in the cylinder.

It is proposed, based on the discussion in Section 3.2.6, that a close estimate of the true tensile strength (f_t) may be obtained from the linear elastic limit state at load level P_I, while also taking into account the correction for the width of the load strip proposed by Tang (1994):

$$f_t = \frac{2P_I}{\pi D}\left[1 - \left(\frac{b_1}{D}\right)^2\right]^{\frac{2}{3}}$$

(4.19)

The values obtained for σ_{Nu} and f_t after correction for statistical outliers are shown in Table 4-5. The values for σ_{Nu} are up to 45 per cent higher than the values for f_t. The correction proposed by Tang (1994) is constant for all results and accounts for only 4 percent of this difference. For the mixes of which enough samples were tested to allow such an analysis, the results of a statistical boxplot test for outliers is shown in Figure 4-14. Based on this analysis a single outlier for D was excluded from the results in the table.

Table 4-5: Tensile splitting test results

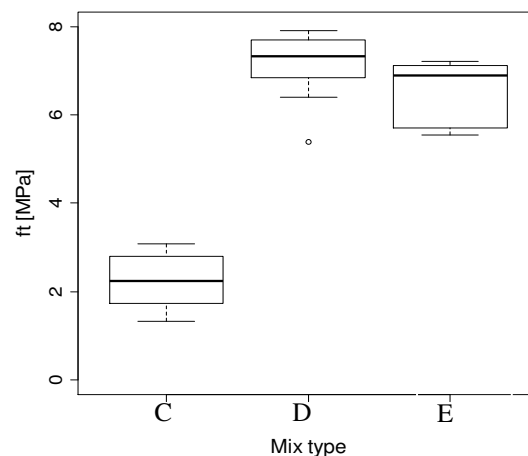| Mix ID	Number of specimens	Peak load [kN]	Std.dev. [kN]	σ_{Nu} [MPa]	f_t [MPa]	Std.dev. [MPa]
Mix A	3	708	18.9	10.01	6.29	0.25
Mix B	3	833	12.5	11.78	6.39	0.33
Mix C	12	164	46.4	2.25	2.23	0.59
Mix D	9	767	29.8	10.86*	7.28*	0.51
Mix E	6	510	42.2	7.21	6.56	0.73

* Outlier omitted

Figure 4-14: Box plot of cylinder splitting results

The adjusted tensile splitting test methodology to determine the tensile strength of fibre reinforced concrete developed as part of this study was published in Denneman et al (2011b).

The fracture mechanism and stress redistribution that leads to the occurrence of the two peaks require further evaluation. As part of the numerical simulation in Chapter 5, the tensile splitting test is modelled in a finite element framework using a fracture mechanics approach.

With both the fracture energy and the tensile strength known, it is possible to create a model of the fracture behaviour of the material. A crack will be induced when the tensile stress reaches the tensile strength of the material. The fracture energy represents the amount of energy that needs to be dissipated to reduce the stress transfer between the cracked faces to zero.

4.5   Analysis of fatigue tests

Cyclic loading tests were performed as part of experimental Phase 2 and 4. In Phase 2 cyclic testing with limited scope was performed on plain concrete beams at UC Davis. The fatigue testing performed in Phase 4 had a wider scope and includes a size effect study on beams as well as tests on disk specimens. The results are presented in terms of the evolution of vertical displacement or CMOD with the increase in number of cycles. Figure 4-15 shows the evolution of the load-CMOD response of a test run at 80 per cent of the monotonic peak load for specimen type TPBF1-C. The results indicate that secant stiffness of the beam reduces with each stress cycle, even at this lower stress level. The displacement consequently increases with every cycle. The results of the cyclic tests, where displacement was successfully recorded are contained in Appendix B. Note that a limited number of data points are recorded per load cycle as result, the peak and minimum load levels are often not visible in the graphs.

4.5.1   Repetitions to failure and size-effect

Fatigue tests are run in load control at a percentage of the monotonic peak load. The number of cycles to failure for the various specimen types tested at the different load levels is shown in Figure 4-16. The results shown are for the plain concrete beams tested as part of phase II, and the different specimen types (beams and disks) tested as part of phase IV. The results

show considerable scatter and only a limited number of tests were performed on the plain concrete samples.
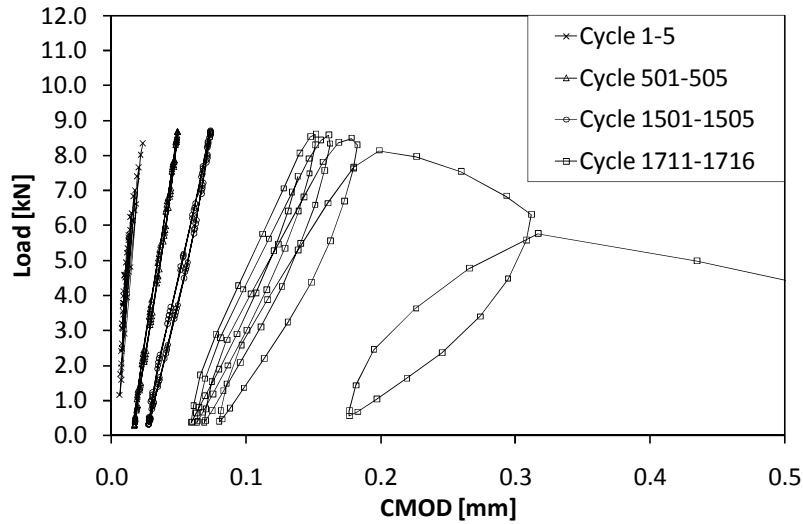

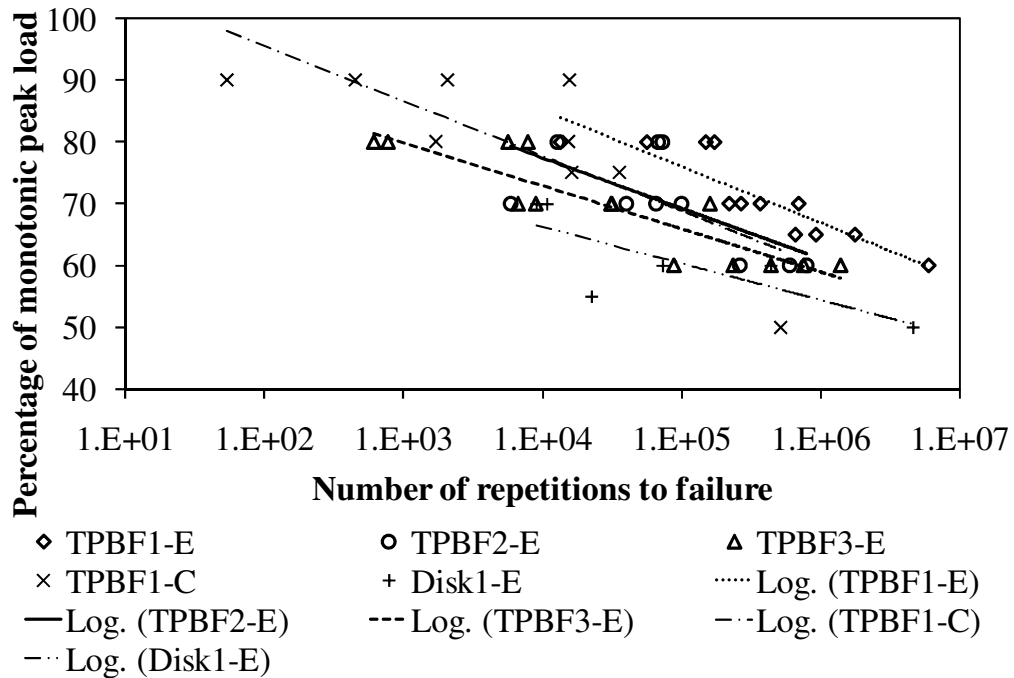**Figure 4-15: Evolution of CMOD in fatigue test on TPBF1-C specimen**

Figure 4-16: Number of repetitions to failure versus percentage peak load

The individual difference in performance between the 50, 100 and 150 mm high beam specimens (TPBF1-E and TPBF2-E) and the disks Disk1-E in Figure 4-16 are caused indirectly by size effect. The MOR for the smaller specimens is relatively higher and these are therefore tested at a higher stress level. If plotted in terms of nominal stress, as shown in Figure 4-17, the difference between the 100 and 150 mm high samples disappears. The trend line for the 50 mm high TPBF3-E specimens still plot below the results for the other sizes. The 50 mm beams may have been weaker due to the small dimensions of the beam cross-section with may have given rise to other sources of size effect as discussed in Section 4.3.

The results in Figure 4-17 do not indicate any significant size effect in the fatigue performance of the fibre concrete material between the beam specimens. The absence of size effect in fatigue would imply a model for fatigue life prediction based on the ratio of MOR approach would yield reliable predictions. Figure 4-17 also shows the results for the disk specimens however. The stresses shown for the disk were calculated using finite element method under the assumption of linear elastic material behaviour. The FEM model is presented in the next chapter. The results show that the disk specimens have superior fatigue performance, if analysed in terms of LE stress condition. These results indicate that the use of the beam results to predict the fatigue performance of slabs using the conventional LE approach would not yield reliable results. This will be discussed in more detail in Chapter 5.
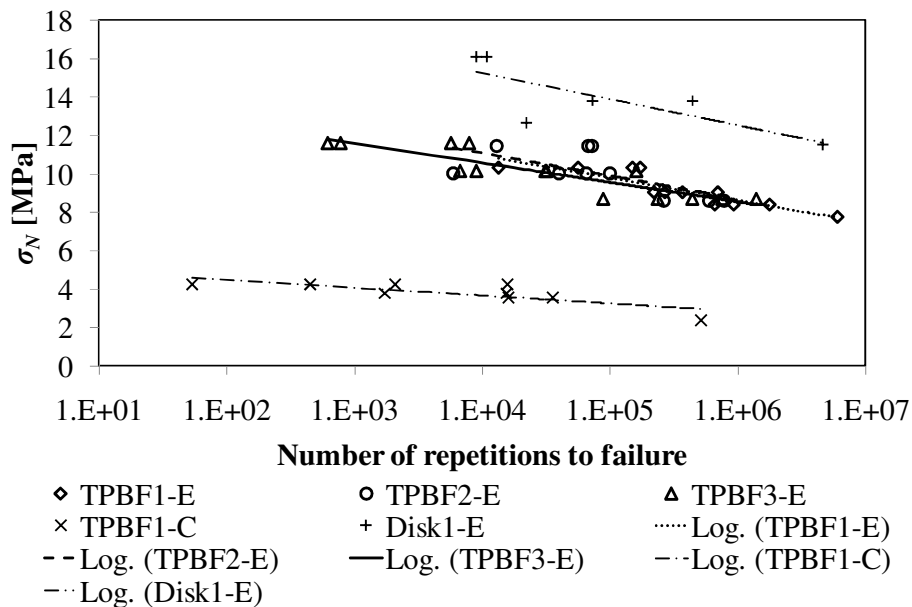

Figure 4-17: Number of repetitions to failure versus nominal stress

The graph in Figure 4-17 shows that the fatigue experiments on both the plain and fibre reinforced concrete, although run at a percentage of the peak load, were performed at a stress level well above the tensile strength values for the material in Table 4-2. This implies that the linear elastic limit state for the specimens is reached in the first load cycle. According to fracture mechanics theory, cracking is induced when the tensile strength is reached. Implying that in these tests fatigue damage was present from the time of the first load application.

4.5.2 Exploring the relationship between monotonic and cyclic tests

As mentioned in Section 2.6.2, the notion proposed by Hordijk (1992), that the monotonic load-displacement curve provides an envelope for fatigue tests has been opposed by later research. There is some evidence from literature that the monotonic curve as an envelope for cyclic tests is a workable model for fibre reinforced concrete. For this reason, the relationship between monotonic and cyclic tests is explored in this section. Figure 4-18 shows a comparison between the monotonic experimental data and the cyclic loading results for TPB tests on plain concrete performed at UC Davis. The results shown in the figure are typical, for both the tests on plain and fibre reinforced concrete performed as part of this study, in that the softening process under cyclic loading continues until the displacement at the peak of the cycle approximately coincides with the envelope of the monotonic load-CMOD curve.
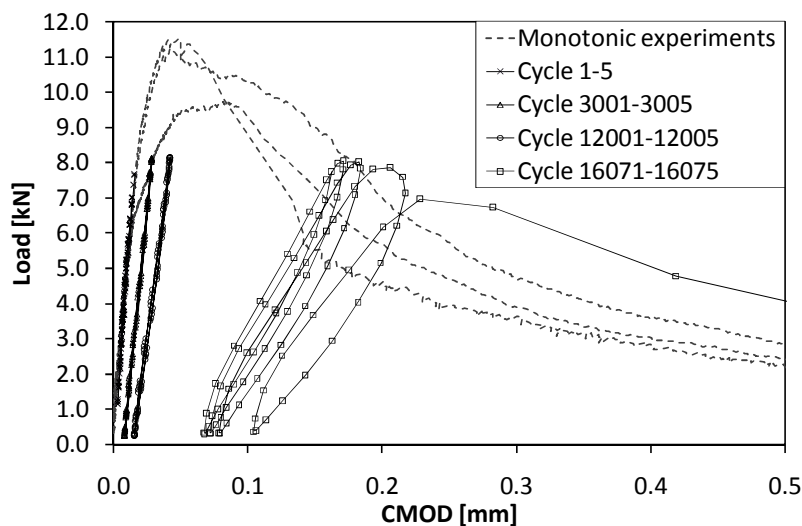

Figure 4-18: Comparison between monotonic and cyclic load-CMOD curves.

Figure 4-19 schematically shows a method which was developed to determine the displacement at which unstable collapse follows in the cyclic experiments. It is necessary to make an approximation of the displacement due to the limited number of data points recorded for each load cycle. As a rule, no data point will be available for the peak of the load cycle. To determine the location of point C in Figure 4-19, representing the displacement at the last cyclic peak load, the secant modulus of the final cycle is estimated. This is then used to obtain the approximate position of point C.
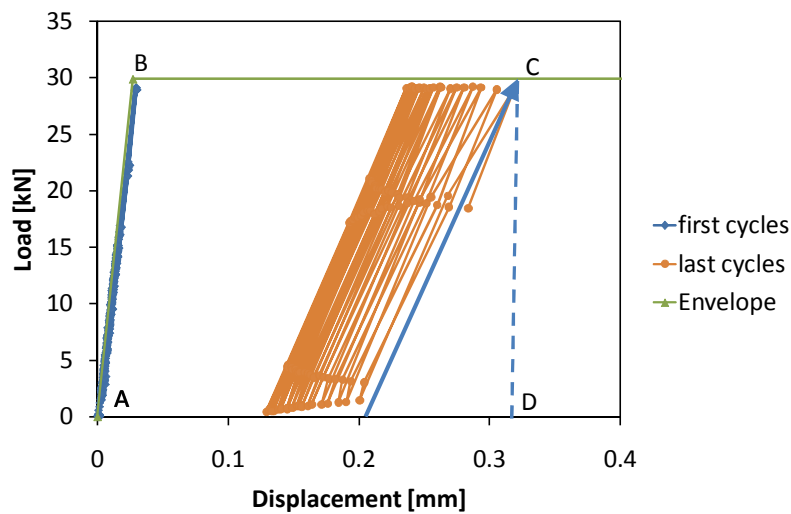

Figure 4-19: Determining displacement at point C and dissipated work of fracture

With point C known, the work of fracture applied in the cyclic loading experiments under stable loading can also be estimated. The work of fracture delivered in the test is obtained from calculating the area ABCD in Figure 4-19. The work of fracture applied up to the induction of unstable failure shall be denoted W_{ff}. The line A-B representing the load-displacement behaviour in the first load cycle is constructed using linear elastic beam theory. The deflection (δ) at the centre of a simply supported beam with two equal loads is obtained from:

$$\delta = \frac{Wx}{24EI}\left(3s^2 - 4x^2\right) \tag{4.20}$$

Where in the case of the FPB experiments W is $P/2$, x is $s/3$ and I is the moment of inertia. Using this equation the deflection at the peak of the first load cycle can be calculated. To

demonstrate that the linear elastic solution approximates the initial response, the load displacement curve for the first five cycles is included in the figure.

Drawing a horizontal line from point B provides an envelope for the load displacement behaviour of the cyclic tests. This envelope is included in the cyclic loading results in Appendix B.

By drawing a vertical line from point C down to the horizontal axis, the area ABCD is completed. This area is W_{ff}, i.e. the work applied from the first load cycle to the last cycle in which the cyclic peak load was reached before unstable failure occurred.

Figure 4-20a shows the position of point C for cyclic tests on plain concrete TPB1-C performed at different stress levels. Figure 4-20b and Figure 4-20c. show similar data for the tests on fibre reinforced concrete FPB3-E and disk1-E specimens.
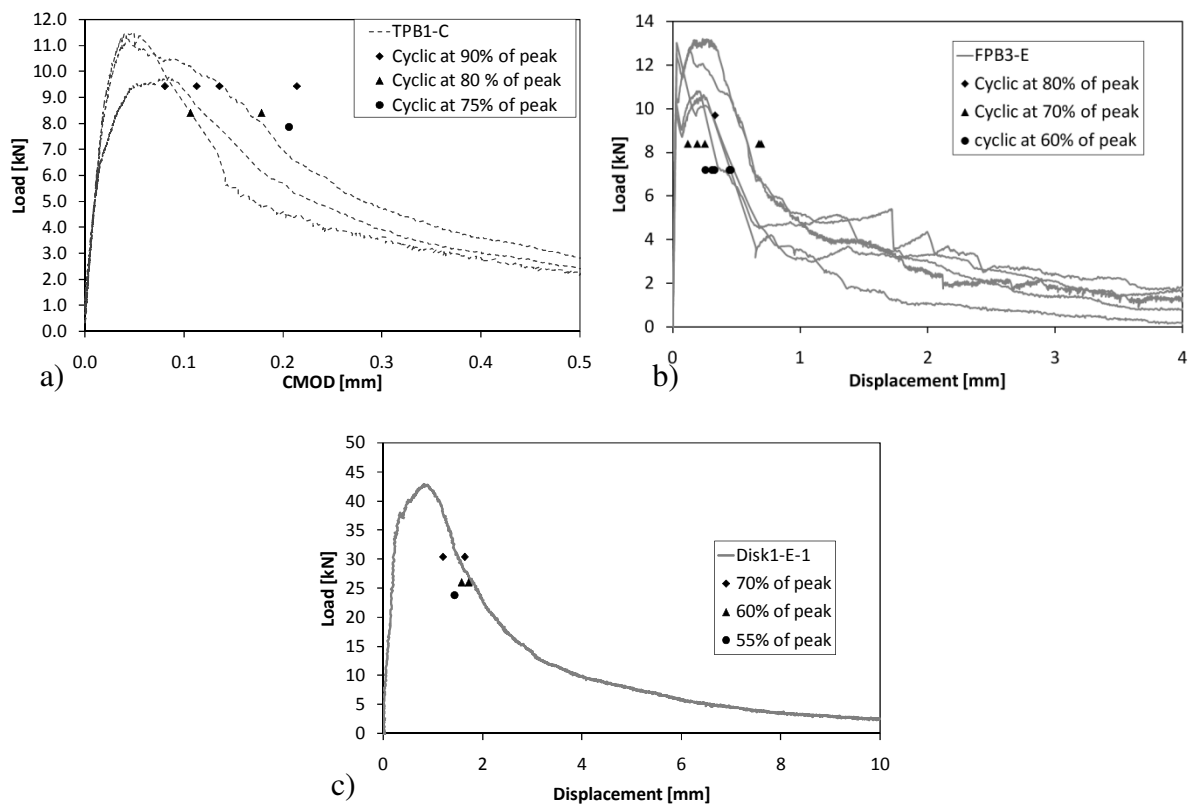

Figure 4-20a: Position of point C for plain concrete TPB1-C specimens, b: position point C for FRC FPB3-E specimens, c: position point C for FRC disk1-E specimens

Unfortunately, a comparison between the monotonic and cyclic results for other Mix E specimen types is not possible, because the monotonic tests failed in a brittle manner just after the peak was reached. Therefore, no reliable load-displacement data is available for the post peak behaviour of the specimens.

The available results are insufficient to reach a conclusion on whether the monotonic curves provide an envelope for the cyclic data. The data does indicate that the spread of the displacement at which unstable fracture is initiated (the spread in the position of point C) is wider than the spread of the monotonic load-displacement curve trajectories. As the combined data for all tests on Mix E beam specimens in Figure 4-21 shows, there is also no clear trend that the unstable failure is initiated at higher deflections for lower stress levels.
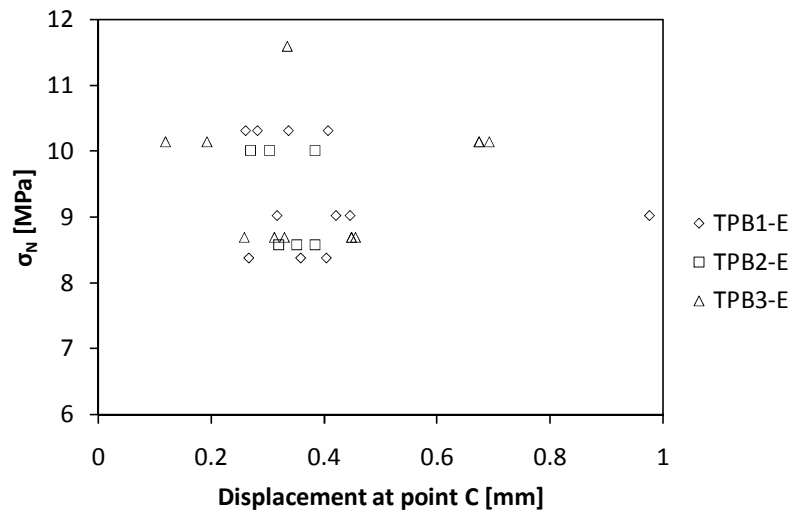

Figure 4-21: Position of point C for cyclic tests on mix E

The work of fracture applied at the induction of unstable failure (W_{ff}) for the different Mix E specimen types is shown in Figure 4-22a. W_{ff} is calculated using the methodology described above and plotted against the nominal maximum stress at which the test was run. The results show that, as expected, the amount of W_{ff} depends on the size of the specimen and geometry. The results can be normalized for the size of the fracture ligament. W_{ff} is divided by the area of the fracture plane in the test yielding an energy equivalent (G_E). Therefore, for the FPB tests G_E is calculated using:

$$G_E = \frac{W_{ff}}{bh} \tag{4.21}$$

For the disk specimens G_E is obtained from:

$$G_E = \frac{W_{ff}}{3Rh} \tag{4.22}$$

Note that the dissipated W_{ff} divided by the area of the fracture ligament does not equate to dissipated fracture energy (G_f) as the specimen is only partially cracked and the softening is unevenly distributed. When the results are normalized for size as shown in Figure 4-22b, the average dissipated work is more or less consistent. In Figure 4-23 the values for G_E at different stress levels are combined in box plots for the different specimen types. The figure shows that the mean value for the mixes is around 1 N/mm for the specimen types tested at various stress levels.
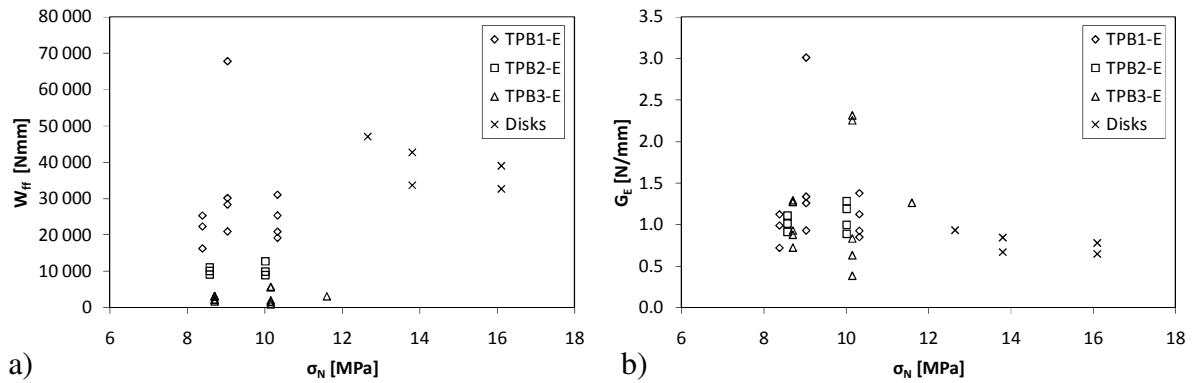

Figure 4-22a: *W_{ff}* **for cyclic tests on Mix E specimens, b:** *G_E* **for cyclic tests on Mix E specimens**
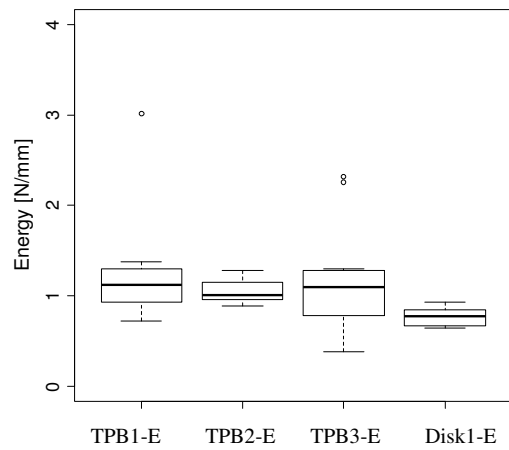
Figure 4-23: Box plot G_E results

In Figure 4-24 the values for G_E are plotted against the number of repetitions to failure. This was done to investigate whether more energy is dissipated in tests ran up to a higher number of repetitions. The outliers identified from the box plot in Figure 4-23 are excluded from this plot. The results indicate that if there is a trend for a higher G_E at higher numbers of repetitions, it is a weak one.
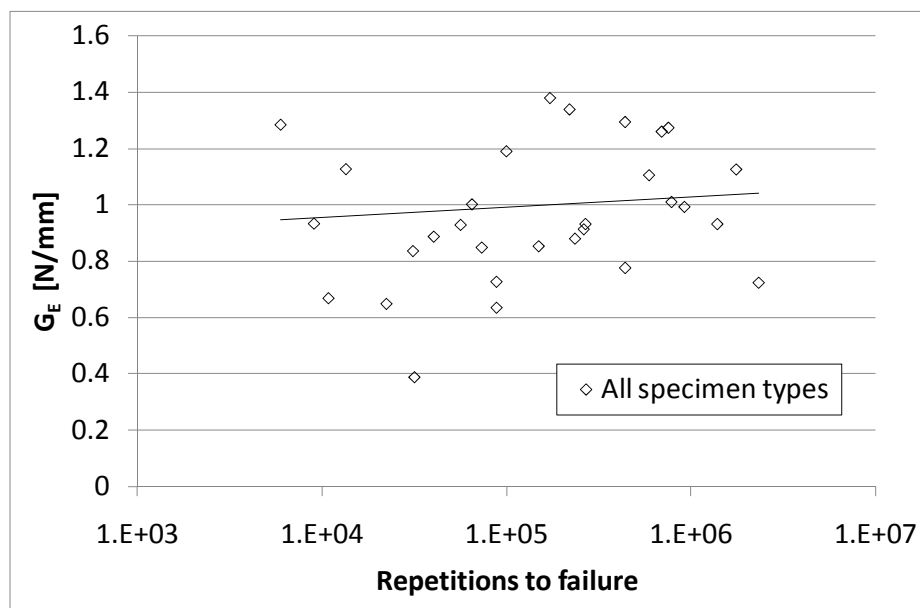

Figure 4-24: Trend of G_E with repetitions to failure

4.6   Discussion of fracture experiments

The testing performed as part of this study had three main aims. The first was to explore the magnitude of the size effect for the material. The second aim was to determine the fracture mechanics material properties required to numerically simulate cracking in the material. The final objective was to compare behaviour of the material under monotonic and cyclic loading, and further to determine fracture properties from the cyclic loading tests that can be used in the prediction of the fatigue performance of the material.

The monotonic testing showed that the material is subject to significant size effect. The implication is that σ_{Nu} or MOR is unsuitable as a design parameter, as the results obtained for a certain specimen size cannot be used to predict the peak load of a specimen with the same geometry, but a different size. σ_{Nu} can therefore not be expected to yield reliable predictions of the bending capacity of a full size pavement. To illustrate this further, a comparison between the LE derived stresses for the beams and the stresses in the centrally loaded disks obtained through LE numerical simulation will be provided in the next chapter.

The magnitude of the size effect in the high performance fibre reinforced concrete was found to be comparable to published values for plain concrete. This highlights the known limitations of the assumption of linear elastic material behaviour in the design of plain concrete pavements, as raised by other researchers and discussed in Chapter 2. For fibre reinforced concrete material under study σ_{Nu} has the added limitation that it does not distinguish between mixes at different fibre contents. The parameter provides an indicator of the nominal peak stress for the material only. It does not provide much indication of the post peak stress capacity of the material. Post peak stress capacity is a key property for fibre reinforced concrete. For fibre reinforced concrete it is important to optimize mixes for post peak toughness rather than for peak strength alone. The post cracking material response needs to be described using a suitable fracture mechanics based parameter, to capture the influence of fibres on the material behaviour under monotonic and cyclic loading.

The above builds a case for the use of a non-linear, fracture mechanics based approach to predict the bending capacity of high performance fibre reinforced structures. Fracture properties that can be used as input to fracture mechanics simulation were determined in this chapter. A method was introduced to model the tail of the load displacement curve in TPB test, in order to obtain the full work of fracture required to completely break the beam. From this, the specific fracture energy for the material was determined. The tensile splitting test

was adjusted to allow the determination of the tensile strength of the fibre reinforced material. It is proposed that a close estimate of the true tensile strength of high performance fibre reinforced concrete may be determined from cylinder splitting tests provided that: measures to reduce size effect are observed, the calculation is corrected for the influence of boundary conditions, and the transversal deformation is measured.

The fracture energy and tensile strength parameters can be used in the definition of a fracture mechanics damage function for the material. The numerical modelling exercise will also serve to further validate the methods of deriving fracture energy and tensile strength introduced in this chapter.

The comparison of results from the monotonic and cyclic flexural tests seems to indicate that the monotonic load-displacement curve may provide an envelope for the evolution of the load-displacement curve under cyclic loading at least at the relatively high stress levels applied as part of this study. The experiments have provided valuable data for the comparison of material response under monotonic and cyclic loading. There is little evidence of size effect in the cyclic test results for beams. The results for the disks however, do indicate that the use of a fatigue function based on the MOR obtained from the beam specimens, will not lead to reliable prediction of the fatigue performance of the disks.

The analysis of the load displacement curves for the fatigue tests resulted in the identification of one parameter that may prove useful in the development of fatigue prediction models. The equivalent energy (G_E) dissipated per unit ligament area is largely consistent regardless of specimen shape and size. The value of this parameter in the prediction of fatigue will be assessed in the next chapter.